Abundance analysis of benchmark M dwarfs

T. Olander[1], U. Heiter[1], N. Piskunov[1], J. Köhler[2], and O. Kochukhov[1]

[1] Observational Astrophysics, Department of Physics and Astronomy, Uppsala University, Box 516, SE-751 20 Uppsala, Sweden,
  e-mail: ulrike.heiter@physics.uu.se
[2] Thüringer Landessternwarte, Sternwarte 5, 07778 Tautenburg, Germany

ABSTRACT

Context. Abundances of M dwarfs, being the most numerous stellar type in the Galaxy, can enhance our understanding of planet formation processes. They can also be used to study the chemical evolution of the Galaxy, where in particular α-capture elements play an important role.
Aims. We aim to obtain abundances for Fe, Ti, and Ca for a small sample of well-known M dwarfs for which interferometric measurements are available. These stars and their abundances are intended to serve as a benchmark for future large-scale spectroscopic studies.
Methods. We analysed spectra obtained with the GIANO-B spectrograph. Turbospectrum and the wrapper TSFitPy were used with MARCS atmospheric models in order to fit synthetic spectra to the observed spectra. We performed a differential abundance analysis in which we also analysed a solar spectrum with the same method and then subtracted the derived abundances line-by-line. The median was taken as the final abundance for each element and each star.
Results. Our abundances of Fe, Ti, and Ca agree mostly within uncertainties when comparing with other values from the literature. However, there are few studies to compare with.

Key words. M dwarfs – spectral synthesis – stellar parameters

1. Introduction

Recent years have shown an increased interest in M dwarfs as they have become favourable targets in the hunt for exoplanets. This is because exoplanets are easier to detect around M dwarfs due to the low mass and faintness of these cool stars, which favours both the radial velocity and the transit methods. Additionally, the proximity between star and potential planet in the habitable zone increases opportunities for characterising the planet by using, for example, transit spectroscopy (cf. e.g. Luque et al. 2021; Cadieux et al. 2022; Loyd et al. 2024).

These cool and faint stars are the most common stars in the galaxy as over 70% of the stars in our galaxy are M dwarfs (Henry et al. 2006). The multitude of M dwarfs could make them important in characterising large stellar structures such as clusters. We are however still limited by our observational capabilities. M dwarfs could also be important for tracing chemical evolution because of their long expected lifetime and slow evolution. They would be an indicator of the local chemical makeup from when a group was formed. The difficulty would be to estimate the M dwarf age but this problem could be solved by studying stars in clusters. The multitude of stars also increases the likelihood of finding a habitable exoplanet as it is estimated that each M dwarf has over two Earth-like exoplanets (Dressing & Charbonneau 2015).

M dwarfs are however difficult targets to observe. The cool temperatures in the photosphere of M dwarfs makes it possible for di-atomic and tri-atomic molecules to form, such as TiO, FeH, H_2O, VO and more (Gray & Corbally 2009). Atomic lines are hidden and blended by these molecular lines. This is especially true in the optical wavelength region where bands of TiO blend with the atomic lines. In the near-infrared (NIR) we find less strong molecular features and the atomic lines are easier to distinguish, but not without issue. For example, in the H-band we find a lot of lines of water molecules which suppress the continuum, forming a pseudo-continuum (Sarmento et al. 2021). There is less water in the J-band but instead telluric lines are imprinted on the spectra when using ground-based observations. One can either ignore the telluric lines and use atomic lines in-between, observe a telluric standard star or use software (as explained later) in order to remove the telluric lines.

Despite these challenges multiple spectroscopic studies have determined effective temperature, metallicity, and surface gravity. A few examples of such studies are Mann et al. (2015), Lindgren et al. (2016); Lindgren & Heiter (2017), Passegger et al. (2018, 2019), Rajpurohit et al. (2018), Sarmento et al. (2021), and Souto et al. (2022). Several of these studies used either calibrations or photometry in order to obtain the surface gravity because of the degeneracy found between the parameters.

It is important to obtain abundances of stars in general, in order to explore and understand galactic chemical evolution. In particular, abundances of α-capture elements allow one to determine the relative contributions of the end stages of different types of masses and thereby the nucleosynthetic history of stellar populations within the Milky Way. Abundances of M dwarfs will also lead to progress in our understanding of planet formation due to the increased number of exoplanets detected around M dwarfs. Key elements in this regard are C, S, O, Na, Si, Fe, Mg, Ni, Ca, and Al (in order from most volatile to most refractory, Wang et al. 2019). By determining the abundances of these elements in a host star and accounting for the depletion of volatiles during the formation of rocky planets the interior compositions and structures of terrestrial exoplanets can be constrained and compared to the Earth.

The ratios of the elemental abundances found in the star are often assumed to be mirrored in the planet (e.g. Thiabaud et al. 2015; Brinkman et al. 2024). However, for some high-density planets indications for differences between the abundances of the planet and the host star have been found (e.g. Santerne et al. 2018). These cases may be used to explore the special conditions required to form Mercury-like planets. Few abundance studies of M dwarfs have been published up to now. Here is a sample with the derived species in parentheses: Woolf & Wallerstein (2005) (Fe and Ti), Tsuji & Nakajima (2016) (C and O), Abia et al. (2020) (Rb, Sr, and Zr), Maldonado et al. (2020) (C, O, Na, Mg, Al, Si, Ca, Sc II, Ti, V, Cr, Mn, Co, Ni, Zn), Shan et al. (2021) (V), Souto et al. (2022) (C, O, Na, Mg, Al, Si, K, Ca, Cr, Mn, Fe, and Ni), Ishikawa et al. (2022) (Na, Mg, Si, K, Ca, Ti, V, Cr, Mn, Fe, and Sr), Melo et al. (2024) (Fe, C, O, Na, Mg, Al, Si, K, Ca, Ti, V, Mn), Jahandar et al. (2025) (Fe, Mg, O, Si, Ca, Ti, Al, Na, C, and K).

When performing abundance analyses it is important to have an accurate effective temperature and surface gravity. In this work we used data obtained with interferometry. With an angular diameter from interferometry and a bolometric flux from photometry, the Stefan-Boltzmann law can be used in order to obtain model-independent effective temperatures. Using distances from astrometry and empirical mass-luminosity relations, the mass and thereby the surface gravity of the star can be obtained. Some interferometric studies of M dwarfs which have been published up to date include Berger et al. (2006); von Braun et al. (2011); Boyajian et al. (2012); von Braun et al. (2014); Kervella et al. (2016); Schaefer et al. (2018); Rabus et al. (2019); Caballero et al. (2022); Ellis (2022).

Many current and future surveys include M dwarfs in their sample, which means that thousands of M dwarfs need to be accurately characterised. APOGEE (Majewski et al. 2017; Jönsson et al. 2020) is a survey primarily targeting red giants but they have also observed M dwarfs. Another example is PLATO (Rauer et al. 2014, 2024), which is a future space telescope that will use light curves in order to detect exoplanets. Thousands of M dwarfs are part of the PLATO sample, and spectra from follow-up observations need to be analysed. New methods using machine learning have been developed in order to facilitate the analysis of large samples of stars such as these. Some examples of such studies are Birky et al. (2020); Passegger et al. (2020, 2022); Rains et al. (2024), and Olander et al. (2025). In some cases the observed spectra of well known stars are used directly in the training and other times they are used in order to verify the results. Due to the difficulties discussed above there has been a lack of well characterised M dwarfs. We have effective temperatures and surface gravity obtained from interferometry for a set of M dwarfs but we also need the metallicity and abundances of various elements, especially the α-elements. This is obtained by carefully analysing high-resolution spectra of individual stars, which has been done by the studies referenced above.

In this article we present an abundance analysis of a sample of M dwarfs with interferometric measurements from Boyajian et al. (2012). In Sect. 2 we introduce our sample and observations. In Sect. 3 we describe our analysis method. In Sect. 4 we present our results followed by a discussion and conclusions in Sect. 5.

2. Sample and observations

The sample of stars presented in this paper consists of well characterised stars with T_{eff} and $\log g$ obtained using interferometry in Boyajian et al. (2012). They obtain T_{eff} by measuring the
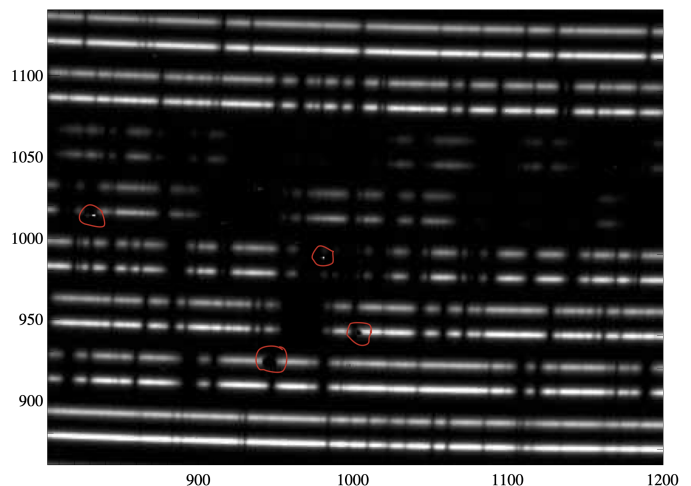
Fig. 1. A fragment of spectra taken at two nodding positions by GIANO-B after combining them. One can see replicated spectral lines corresponding to the same spectral orders, the tilt of the slit image, a couple of strong cosmic ray hits and some detector defects outlined in red.

limb-darkened angular diameter with the CHARA array and using the bolometric flux obtained from Hipparcos parallaxes (van Leeuwen 2007) and photometry fitted to spectral templates in the Stephan-Boltzmann law. The surface gravity is obtained using an absolute K-band mass-luminosity relation from Henry & McCarthy (1993). The sample consists of nine stars and includes one binary system. The stars are from spectral type M1 to M4 and in the literature the majority have a sub-solar metallicity. The sample can be seen in Table 1 together with the total exposure time and the signal-to-noise ratio (SNR). The SNR is given at 11785 Å, which corresponds to the centre of the part of the spectra used in this article (centre of order 65, see Sect. 2.2). In case of multiple observations per star (two for GJ 412A, GJ 699, and GJ 725A; four for GJ 436), which were co-added after data reduction during telluric removal (see Sect. 2.3), the SNR is the square root of the sum of the squared SNRs of each observation.

2.1. Observational data

The observations were performed with the GIANO-B spectrograph mounted on the 3.58 m Telescopio Nazionale Galileo on La Palma. GIANO-B is a near-infrared echelle spectrograph with a resolving power of 50 000 and a wavelength coverage from 9000 to 24 500 Å (Origlia et al. 2014). Observations were conducted on 25 to 27 May 2019 in visitor mode. The observations were planned with the goal of achieving an SNR of at least 150.

2.2. Data reduction

The focal plane format of GIANO-B represents a challenge for data reduction due to 50 curved spectral orders present in two nodding positions, multiple detector defects, variable tilt of the slit images, etc., as illustrated in Fig. 1, where artefacts are marked in red. We have selected to use the REDUCE package (Piskunov & Valenti 2002; Piskunov et al. 2021), which is well tested on several instruments. This includes the ESO VLT CRIRES+ spectrograph, which has a number of similarities with GIANO-B. After constructing a master flat, tracing spectral orders, and extracting the wavelength calibrations (UNe calibra-

Table 1. Target sample.

Name	Simbad identifier	Sp type	RA	DEC	K mag	Exp. time [s]	SNR
GJ 411	HD 95735	M2+V	11 03 20.1948	+35 58 11.576	3.340	120	281
GJ 412A	BD+44 2051	M1.0V	11 05 28.5769	+43 31 36.386	4.769	600	293
GJ 436	Ross 905	M3V	11 42 11.0933	+26 42 23.650	6.073	1600	274
GJ 526	HD 119850	M2V	13 45 43.7755	+14 53 29.471	4.415	200	216
GJ 581	BD−07 4003	M3V	15 19 26.8269	−07 43 20.189	5.837	600	181
GJ 699	Barnard's star	M4V	17 57 48.4984	+04 41 36.113	4.524	320	190
GJ 725A	HD 173739	M3V	18 42 46.7043	+59 37 49.409	4.432	240	172
GJ 725B	HD 173740	M3.5V	18 42 46.8946	+59 37 36.721	5.000	600	224
GJ 809	HD 199305	M1.0V	20 53 19.7889	+62 09 15.817	4.618	400	210

Notes. Data were obtained from Simbad using the Python module astroquery.simbad. Exp. time is total time on target (both A and B nodding positions and sum of individual exposures in the case of multiple observations). See text for specification of signal-to-noise ratio (SNR).

tion lamp) we combined the raw frames from the A and B nodding positions and extracted them as one frame, accounting for the slit tilt. The slit orientation was mapped from the UNe frames and then used for the optimal extraction of the science spectra as described in Piskunov et al. (2021). Continuum normalisation in REDUCE requires wavelength overlap between orders, which forced us to restrict the data reduction to the 36 bluest orders (9400 to 17000 Å), and here we encountered the biggest challenge in our reduction. The usual initial guess for the continuum fit required for order splicing is the blaze functions, derived from the master flat. These show pronounced fringing with an amplitude of a few percent and a frequency comparable to the width of the spectral lines. To resolve this problem we first fitted a "continuum" to the blaze functions not affected by telluric absorption, then fitted a 2D surface to the upper envelope of the spectral format by associating each blaze point with its position on the detector and interpolating to the orders affected by tellurics. The corrected set of blaze functions was good enough to produce a decent continuum fit for orders 45 to 80 that are used in this article.

2.3. Telluric removal

Telluric lines were removed using an updated version of the software viper[1] (Velocity and IP EstimatoR, Zechmeister et al. 2021). The main concept of viper is based on the method described by Butler et al. (1996). The algorithm has been extended by adding a term for the telluric spectrum, which enables its usage for observations taken in the NIR. Using least-squares fitting, the wavelength solution, blaze, instrument profile and telluric line depths of the observations are modelled simultaneously to account for instrument instabilities and weather changes. Although viper was originally developed for the determination of radial velocities (RVs), it can also be used for pure telluric correction. For the telluric forward modelling viper uses synthetic standard models obtained from Molecfit (Smette et al. 2015) for each molecule in the Earth atmosphere. For details regarding the telluric removal the reader is directed to Köhler & viper Pipeline Team (2024).

We fed viper with pre-normalised spectra and adjusted the settings in order to obtain the best possible telluric removal. Still we faced problems in the removal of deep tellurics, which cannot be accurately modelled. However, we avoided spectral lines blended with or those that are near strong telluric lines in our analysis. In cases where we have multiple observations for the

same star the spectra were co-added within viper, by using a weighted average of all the telluric-corrected spectra.

3. Method

For the analysis we used Turbospectrum (Alvarez & Plez 1998; Plez 2012; Gerber et al. 2023) together with the wrapper TSFitPy (Gerber et al. 2023; Storm & Bergemann 2023) and MARCS atmospheric models (Gustafsson et al. 2008). It uses the Bergemann et al. (2021) and Magg et al. (2022) solar abundances. TSFitPy fits synthetic spectra generated by Turbospectrum to observed spectra using Nelder-Mead minimisation. In this work we use line-by-line fitting and thereby obtain abundances for each line. In order to minimise the effects from used models we perform a differential abundance analysis. We analyse the high resolution solar spectrum provided by Reiners et al. (2016) using the same method as for the M dwarfs. The one difference was that the solar metallicity was always set to zero and we did not alter the Ti and Ca abundances. The other parameters were set to $T_{\rm eff}$: 5771 K and log g: 4.44 dex[2]. We then subtract the solar abundance for each line from the M dwarf abundance for the same line. The solar spectrum was obtained using a Fourier transform spectrograph (FTS) and the resolution in the NIR was 10^6.

For the M dwarf input parameters we used Boyajian et al. (2012) for $T_{\rm eff}$ as well as radius and mass to calculate log g. The exception is the binary GJ 725A and B where we used Mann et al. (2015). There is an inconsistency for the parameters from Boyajian et al. (2012) for the B star. The effective temperature for that star differs significantly from other measurements which indicates a possible issue with the measured angular diameter. This has been seen for example in Souto et al. (2020) and Olander et al. (2025). For projected equatorial rotational velocity $v \sin i$ and radial velocity RV we used Reiners et al. (2018) and Fouqué et al. (2018). The rotational velocity was fixed throughout the analysis, and set to the upper limit given in the references. Our sample consists of slowly rotating stars and the effect from magnetic broadening should therefore be minimal. We note that our models do not include broadening caused by magnetic fields. The radial velocity is allowed to be adjusted slightly for a better fit. This is done by a second fitting after the abundance, see Storm & Bergemann (2023) for more details. For the results presented in this work the radial velocity rarely shifted by more than 2 km s^{-1}. For input metallicity [Fe/H] we used Mann

---

[1] https://mzechmeister.github.io/viper_RV_pipeline

[2] The units of surface gravity are cm s^{-2}. However, throughout the article, we use the unit dex when specifying values of log g.

et al. (2015). TSFitPy calculates the microturbulence V_{turb} using an empirical relation based on T_{eff}, $\log g$, and [Fe/H][3], which was derived for the data analysis within the Gaia-ESO Public Spectroscopic Survey (M. Bergemann, priv. comm.). We set the macroturbulence as free. The adopted input parameters are given in Table 2.

3.1. Line data and mask

The abundances determined in this work are based on carefully selected individual atomic lines most suitable for the purpose. However, for a realistic synthetic spectrum calculation including background lines and blends we need information on all transitions, as far as possible, contributing to the spectrum in the observed wavelength range in the stars of interest. At the same time, for an efficient spectrum calculation we want to avoid treating unnecessary transitions. Our line list was thus constructed to include atomic lines relevant for stellar parameters encompassing those of the target stars. For this purpose, we used the VALD database (Piskunov et al. 1995; Ryabchikova et al. 2015; Pakhomov et al. 2019) and its "Extract Stellar" mode. The VALD extraction was done on 10 April 2024 using version 3735 of the VALD3 database and software and the default configuration.

We downloaded two line lists between 10 000 and 14 000 Å, one for an effective temperature of 3000 K and a surface gravity of 4.5 dex, and another for T_{eff}=4000 K and $\log g$=5.5 dex. We used the same minimum threshold for central line depth of 0.001[4], a microturbulence of 2 km s^{-1} and elemental abundances enhanced by 0.5 dex for the extraction of both lists. The lists were subsequently merged by removing duplicates. Detailed information about those individual lines which were analysed including references can be found in Table A.1 in the appendix. In addition to atomic data, we also included molecular data. The data used for the molecular lines were the same as in Bergemann et al. (2012), and they were obtained from Bertrand Plez in private communication. We note that for the calculation of the synthetic spectrum in the fitting process all of the atomic transitions extracted from VALD were used (about 1000 in the wavelength range covered by the analysed lines) together with the molecular data.

A line mask was created for each atomic species by visually inspecting an M dwarf spectrum and the solar spectrum. The mask covers the deepest flux point of the observed line and stretches in general from the central wavelength given in the line list to the nearest local maximum to both left and right. Lines blended with telluric lines and other atomic lines were avoided. The cores of the included lines had to be clearly separated from other line cores, which was assessed on a line by line basis. The software iSpec (Blanco-Cuaresma et al. 2014; Blanco-Cuaresma 2019) was used for producing the line masks. The lines used for each star and each element are listed in Tables A.2 to Tables A.4 in the appendix.

3.2. Metallicity and abundances

We fit for the abundances of Fe, Ti, and Ca, one at a time in an iterative process as follows. We first fit for Fe in order to get the

overall metallicity which is then fixed for the rest of the analysis. We then fit for Ti and thereafter Ca with the previously derived Ti fixed. We then go back to Ti with Ca fixed and the old Ti as an input parameter. We then analyse Ca again with the last Ti fixed and the previous Ca abundance as an input parameter. This iterative process was done in order to break possible degeneracies and dependencies between the abundances. Between each iteration we visually inspected the best fit synthetic spectra and discarded lines that showed a bad fit. This was done by first discarding observed lines containing artefacts. Then we removed lines where the derived abundance was outside of 1 to 2 standard deviations from the median value. Which tolerance was used depended on the number of available lines. If there were few lines we were more forgiving. The final abundance in each iteration was obtained by taking the median of the abundances derived for the acceptable lines. We obtained the uncertainty in the derived abundances by calculating the median absolute difference (MAD) between the different abundances for each individual line after subtracting the corresponding solar abundances.

4. Results

We present our results in Table 3. For some of the stars our uncertainties are high, this is due to a large spread in derived abundances from the different lines. Which lines were used in the fitting procedure for each star can be seen in Appendix A. An example of best fitted lines for Fe, Ti, and Ca can be seen in Figs. 2, 3, and 4. In the figures we plot the output synthetic spectra from TSFitPy. We note that for the construction of the figures the observed spectra were only adjusted according to the literature radial velocity and not what the individual lines were fitted for, which is why they do not always line up. In some cases very weak lines in either the solar or M dwarfs spectra were used in order to increase the number of used lines. The line had to have more than five data points and be clearly visible in comparison to the noise level. An example of this can be seen in Fig. 3 in the last panel were the line in the solar spectrum is really weak. The line is clear when zoomed in more. As can be seen in Figs. 2 to 4 the fit of the lines in both the Sun and in the M dwarf are good. In some cases the line core is not correctly fitted as can be seen for the Ti line at 10496 Å or at 10661 Å in Fig. 3 or the Ca line in Fig. 4 at 10344 Å. This is an issue for some Ti and Ca lines. The cause could be incorrect atomic data or departure from local thermodynamic equilibrium, non-LTE, see more in Sect. 5.

In Fig. 5 we compare with the overlapping sample of Ishikawa et al. (2022), Jahandar et al. (2025), Maldonado et al. (2020), and Souto et al. (2022). In the case of [Fe/H] we are also including Mann et al. (2015) which we used for input metallicity. Ishikawa et al. (2022) used spectra from the IRD instrument mounted on the Subaru telescope. They generated synthetic spectra using MARCS atmospheric models and line lists from VALD and matched the equivalent width of the observed spectra with that of the synthetic. Jahandar et al. (2025) used high resolution spectra from CFHT/SPIRou and the PHOENIX-ACES grid of synthetic spectra and determined T_{eff} and $\log g$ prior to the abundances. Maldonado et al. (2020) used archival HARPS and HARPS-N data. They obtained T_{eff} and metallicity using equivalent widths (msdlines) and $\log g$ from mass-radius relations. To get abundances they used a principal component analysis. We are grouping Souto et al. (2022) and Melo et al. (2024) together as they use the same method and spectra. They analysed APOGEE spectra using Turbospectrum and MARCS atmospheric models with the BACCHUS wrapper. They obtained T_{eff}, $\log g$, [Fe/H], and oxygen and carbon abundances by using so-called T_{eff}-A(O)

---

[3] $V_{turb} = 1.05 + 2.51 \times 10^{-4}(T_{eff} - t0) + 1.5 \times 10^{-7}(5250 - t0)^2 - 0.14(\log g - g0) - 0.005(\log g - g0)^2 + 0.05[Fe/H] + 0.01[Fe/H]^2$, where $t0 = 5500$ and $g0 = 4$.

[4] We note that the central line depth is estimated by the VALD software for extraction, without applying any instrumental or rotational broadening. This information is however not used in the further analysis.

Table 2. Stellar parameters used as input data.

Star	$T_{\rm eff}$ [K]	$\log g$ [dex]	[Fe/H] [dex]	$v \sin i$ [km s^{-1}]	RV [km s^{-1}]	Ref
GJ 411	3465	4.856	−0.38	<2	−84.835	1, 3
GJ 412A	3497	4.843	−0.37	<2	68.760	1, 3
GJ 436	3416	4.796	0.01	<2	9.482	1, 3
GJ 526	3618	4.784	−0.31	<2	15.685	1, 3
GJ 581	3442	4.959	−0.15	<2	−9.530	1, 3
GJ 699	3224	5.059	−0.40	<2	−110.579	1, 3
GJ 725A	3441	4.871	−0.23	2.1	−0.580	2, 4
GJ 725B	3345	4.960	−0.30	2.4	1.190	2, 4
GJ 809	3692	4.719	−0.06	<2	−17.320	1, 3

References. (1) Boyajian et al. (2012); (2) Mann et al. (2015); (3) Reiners et al. (2018); (4) Fouqué et al. (2018)
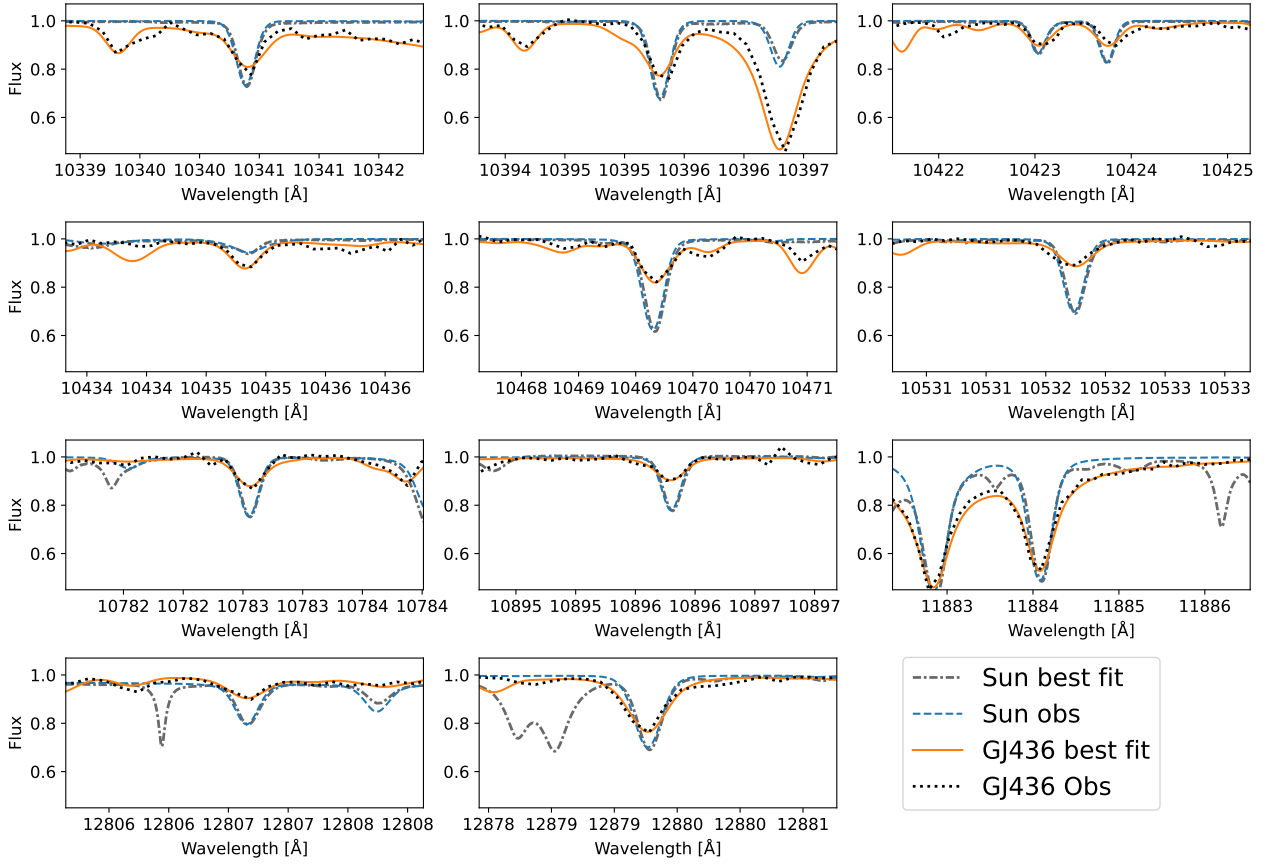

Fig. 2. Best-fitted Fe I lines in GJ 436 and the Sun. The observed spectra were only adjusted according to the literature radial velocity and not the RV fit for individual lines. The wavelength range 10 421 Å to 10 425 Å has two Fe lines. In the other subplots the Fe line is in the middle of the plot.

and log g-A(O) pairs. They also obtained abundances of various atomic species by fitting individual lines.

In Fig. 5 we show [Fe/H] on the left, [Ti/H] in the middle, and [Ca/H] on the right. On the y-axis we show our results and on the x-axis the literature results. The error bars show the uncertainties. In each panel, the name if the star at the different horizontal levels can be found to the furthest right.

Our derived [Fe/H] agree within uncertainties with Mann et al. (2015) (brown star symbols). One outlier is GJ 809 where we derived 0.221 dex and Mann et al. (2015) −0.06 dex. None of the other studies we are comparing with in the figure includes this star. However, Passegger et al. (2019) who used CARMENES spectra and PHOENIX-ACES models obtained 0.29 dex for the same star when using the combined visual and NIR data. When comparing with the literature values for all of the other stars we mostly agree within uncertainties. The general trend is that our [Fe/H] is lower than the literature values. The spread is largest when comparing with Maldonado et al. (2020). Two outliers are GJ 412A and GJ 699. For GJ 412A we derived −0.45 dex and Maldonado et al. (2020) obtained −0.78 dex. However, Mann et al. (2015) obtained −0.37 dex and Souto et al. (2022) −0.40 dex which we agree better with. Our derived
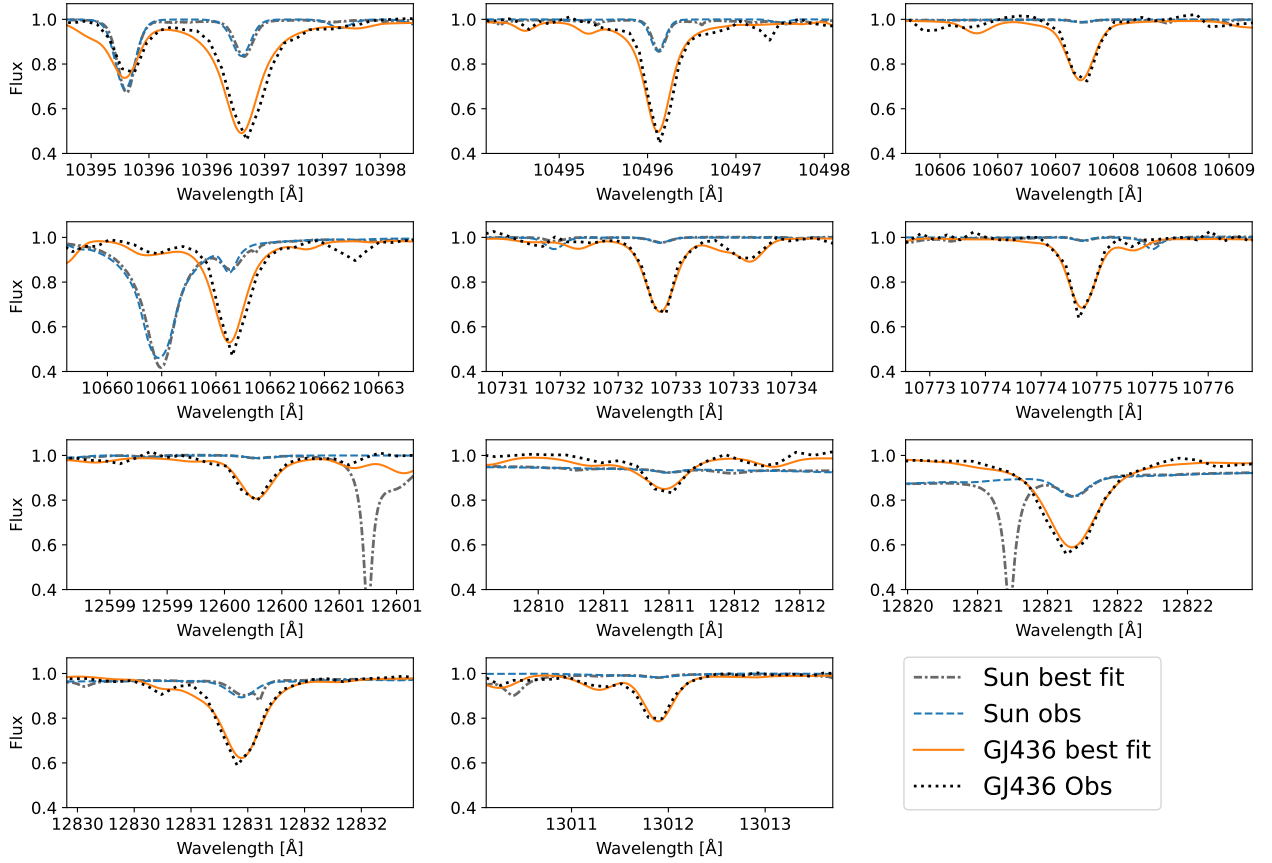
Fig. 3. Same as Fig. 2, for Ti I lines.

Table 3. Abundance ratios with uncertainties.

| Star	[Fe/H]	[Ti/Fe]	[Ca/Fe]	[Ti/H]	[Ca/H]
GJ 411	−0.373 ± 0.143	+0.084 ± 0.172	−0.079 ± 0.193	−0.289 ± 0.224	−0.452 ± 0.240
GJ 412A	−0.451 ± 0.209	+0.094 ± 0.144	−0.027 ± 0.180	−0.357 ± 0.254	−0.478 ± 0.276
GJ 436	−0.010 ± 0.131	+0.110 ± 0.111	+0.052 ± 0.108	+0.100 ± 0.172	+0.042 ± 0.170
GJ 526	−0.162 ± 0.183	+0.172 ± 0.093	−0.094 ± 0.153	+0.010 ± 0.205	−0.256 ± 0.239
GJ 581	−0.151 ± 0.259	+0.186 ± 0.158	−0.012 ± 0.084	+0.035 ± 0.303	−0.163 ± 0.272
GJ 699	−0.582 ± 0.182	−0.009 ± 0.214	+0.086 ± 0.133	−0.591 ± 0.281	−0.496 ± 0.225
GJ 725A	−0.477 ± 0.259	+0.028 ± 0.104	+0.041 ± 0.062	−0.449 ± 0.279	−0.436 ± 0.266
GJ 725B	−0.329 ± 0.202	+0.057 ± 0.134	−0.067 ± 0.075	−0.272 ± 0.242	−0.396 ± 0.215
GJ 809	+0.221 ± 0.158	+0.081 ± 0.087	−0.195 ± 0.054	+0.302 ± 0.180	+0.026 ± 0.167

Notes. Uncertainties (MAD) are given as ± values.

[Fe/H] for GJ 699 is significantly lower than three of the studies, −0.58 dex compared with −0.28, −0.34, and −0.40 (Maldonado et al. 2020, Jahandar et al. 2025, and Mann et al. 2015). However, Ishikawa et al. (2022) obtained −0.60 dex. Passegger et al. (2019) obtained −0.09 when using the combined wavelength regions, and −0.13 and −0.14 dex when using the NIR or the visual alone, respectively. It is clear that this star needs further studies. We note that GJ 699 had the fewest Fe lines used in the fitting (seven).

In the middle panel we show the comparison with [Ti/H]. We agree within the uncertainties when comparing with Melo et al. (2024), Ishikawa et al. (2022), and Jahandar et al. (2025). When comparing with Maldonado et al. (2020) we find a bigger discrepancy, especially at lower [Ti/H]. One outlier is the

star GJ 699 where we derived −0.591 dex and Maldonado et al. (2020) −0.130 dex. Another example is GJ 725A. We note that these two stars show some of the largest differences in [Fe/H] when comparing with Mann et al. (2015). The code used in this work provides the abundance in relation to Fe and it is therefore possible that the discrepancy we see in [Ti/H] is hereditary from [Fe/H]. In order to decipher if this is the case further study is needed, which is outside the scope if this paper.

The right panel shows the result for [Ca/H] and here the spread is larger when comparing with all of the literature values. Here our uncertainties are even larger. This is most likely because we had problems fitting the cores of some of the lines as mentioned earlier. One possible explanation for this bad fit could be non-LTE effects, especially in the solar spectrum. We
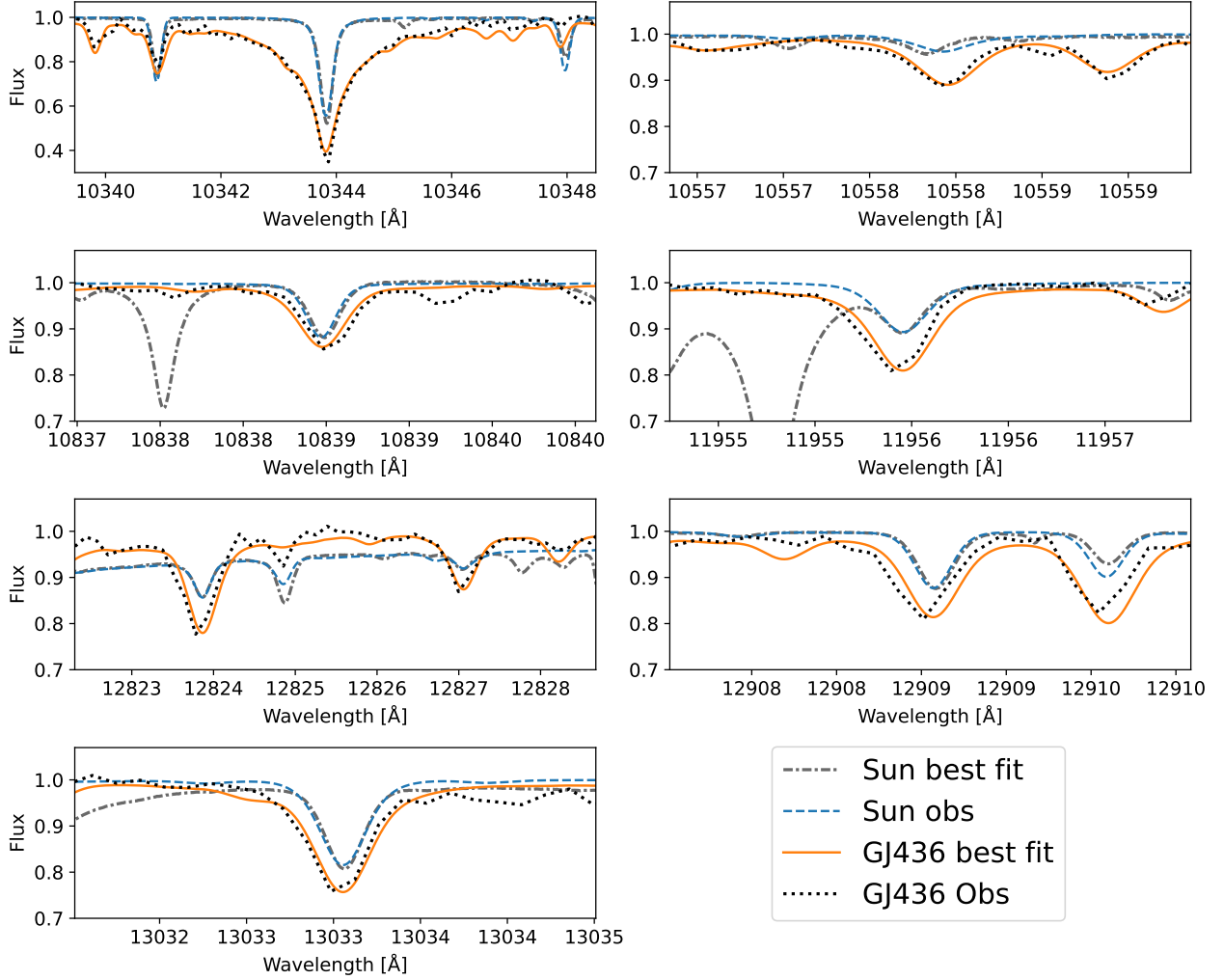
Fig. 4. Same as Fig. 2, for Ca I lines. The wavelength range 12 822 Å to 12 829 Å has two Ca lines. In the other subplots the Ca line is in the middle of the plot.
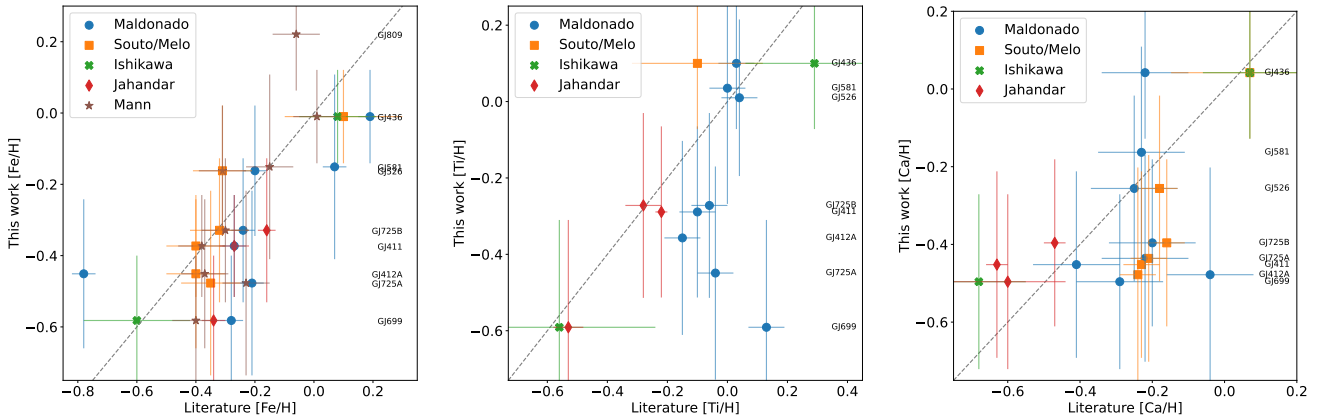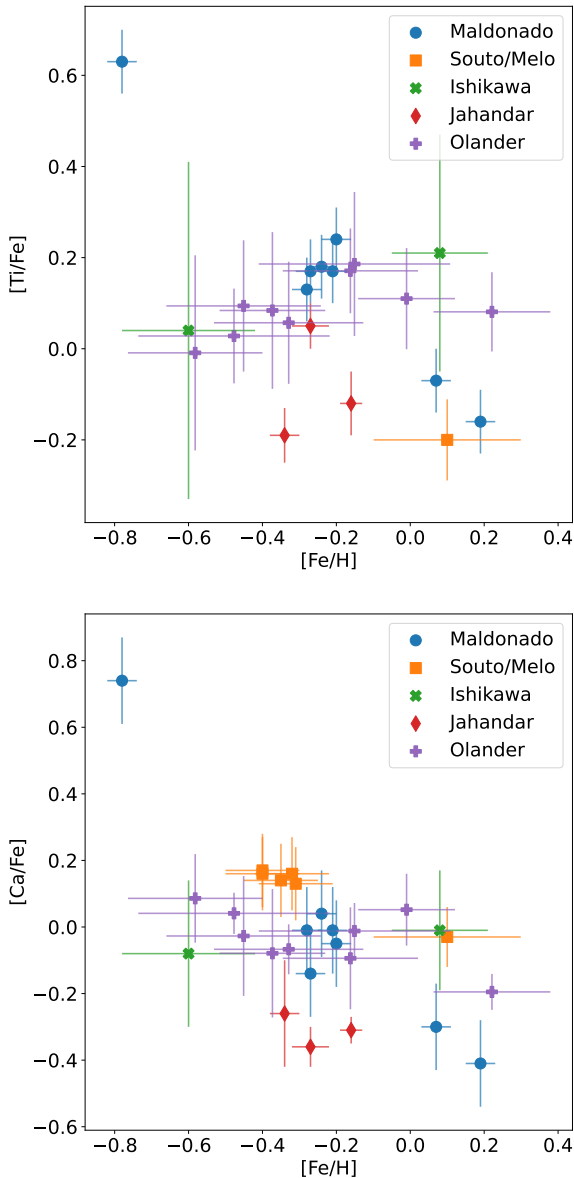

Fig. 5. Abundances from this work vs abundances from the literature for stars in overlapping samples. The same star can be found on the same horizontal line with the name of the star to the right in each figure.

find a clear offset when comparing with Souto et al. (2022) and Melo et al. (2024) where our derived abundances are 0.2 dex lower than those of these authors. The largest spread is found when comparing with Maldonado et al. (2020). GJ 412A is again an outlier when comparing with Maldonado et al. (2020) where

they derived −0.04 dex and we derived −0.478 dex. Souto et al. (2022) derived an abundance of −0.24 dex.

In Fig. 6 we plot [Ti/Fe] and [Ca/Fe] against [Fe/H] for all the stars in the overlapping sample with the literature studies. The symbols are the same as in Fig. 5. For both [Ti/Fe] and

Fig. 6. Abundances of Ti and Ca vs Fe for stars in the sample overlapping with studies from the literature.

our [Fe/H] is close to the Souto et al. (2022) value (−0.33 dex compared to −0.32 dex). It is the A star that differs (−0.48 dex). We note that different spectral lines were used in the fitting of the A star and B star, this can be seen in Table A.2. When we look at the [Ti/H] and [Ca/H] derived for the binary, the difference in abundance between the two binary stars is larger than it is for [Ti/Fe] and [Ca/Fe]. This indicates that it might be the iron abundance for GJ 725A that is problematic. One possible explanation for the much lower [Fe/H] in the A star compared to the B star is the quality of the spectrum. As can be seen in Table 1 the SNR of GJ 725A is lower than that of GJ 725B. A more extended analysis of this binary system is needed.

5. Discussion and conclusions

We have successfully used Turbospectrum with MARCS atmospheric models in the wrapper TSFitPy to derive abundances of Fe, Ti, and Ca for a small set of benchmark M dwarfs. We performed a differential abundance analysis with respect to the Sun in order to minimise model dependence. The analysis was performed line-by-line and the fitted lines were carefully inspected visually. The fit of the used atomic lines are good but some of the uncertainties are high. This is partly due to problems with fringing in the observed spectra but it could also be due to the large gap between spectral type (Sun and M dwarf). The fringing caused an incorrect continuum placement for some of the lines and the resulting abundance for a line could therefore either be too high or too low for those particular lines. We discarded some lines because of issues with the continuum placement. Spectra without fringing would produce a better result with lower uncertainties.

A differential abundance analysis minimises the model dependence of the analysis. However, Gustafsson (1989) discusses that a differential abundance analysis performs better when the analysis is done step-wise if the gap in spectral type is large. The ideal way to analyse an M dwarf would then be to analyse the Sun (G-type), a well known K-type star relative to the Sun, and then the M dwarf relative to the K-type star. This would also make it easier to analyse further elements, for example Si. Upon inspection of the spectra in our study it was found that the available Si lines in the wavelength region we are analysing are strong in the Sun but weak in M dwarfs. The opposite was true for the Ti lines but in the case of Ti we found a sufficient number of suitable lines to fit. Another way to improve the differential abundance analysis would be to use spectra obtained with the same instrument for all types of stars. This would minimise instrumental effects.

Another possible contributor to the high uncertainties is that we discarded strong lines because of a poor fit between the synthetic and the observed lines. The synthetic lines were either too strong or too weak and those lines were therefore discarded from the analysis because of derived abundances outside of the accepted range for that star, see Sect. 3. The reason for the bad fit is unknown but one possible explanation could be incorrect atomic data. We used a generic line list from VALD which means that no astrophysical corrections of the log gf values were made. Even if the effect of the line list is minimised by the differential abundance analysis the results would improve with a line list with astrophysically corrected log gf values, which was out of scope in this paper. Additionally, with a line list optimised for M dwarfs a differential abundance analysis would not be as necessary.

Our results show a somewhat large spread in comparison with literature values. However, there is also a spread when comparing the different literature values with each other. This can be

[Ca/Fe] we have a large spread and none of the studies we compare with really line up well with each other. However the sample here is too small to derive any concrete conclusion regarding trends between the compared studies.

We have one binary system in the sample, GJ 725 A and B. Binaries are expected to have the same abundances as they were formed from the same molecular cloud. For [Fe/H] we differ by approximately 0.15 dex between the stars in the binary, for [Ti/Fe] by 0.03 dex, and for [Ca/Fe] by 0.1 dex. Among the literature studies we are comparing with Maldonado et al. (2020) and Souto et al. (2022) analysed both stars in the binary system. Maldonado et al. (2020) obtained a difference between the A and B components of 0.03 dex for [Fe/H], 0.01 dex for [Ti/Fe] and 0.05 dex for [Ca/Fe]. Souto et al. (2022) obtained a difference of 0.03 dex for [Fe/H] and 0.02 dex for [Ca/Fe] (Ti was not measured for these stars by Souto et al. 2022). The difference we see in abundances between the stars in the binary is an indicator of a high uncertainty in our derived abundances. For the B star

clearly seen in Fig. 6. The figure shows the overlapping sample of stars meaning that it is the same set of stars. We can see that the result from the included studies differ outside of uncertainties which indicates that the uncertainties are underestimated in many studies. The spectroscopic community needs to put more effort into analysing M dwarfs in order to obtain fundamental parameters and abundances. We also need to explore and find the reasons for the differentiating results. Doing this would help our understanding of M dwarfs and the physical conditions inside their atmospheres. Additionally, more abundance analysis studies for a large quantity of M dwarfs are needed in order to draw any conclusions regarding M dwarf abundances in connection to Galactic chemical trends. Souto et al. (2022) state that their Ca abundances agree with the Galactic trend, with [Ca/Fe] increasing towards lower [Fe/H]. The [Ca/Fe] values derived in this work in general follow this trend. This can be seen in the lower panel of Fig. 6, where our values (purple pluses) are higher at lower [Fe/H] and lower at higher [Fe/H]. However, our sample is too small for us to say whether M dwarfs in general follow the Galactic trend of [Ca/Fe].

For some of the lines included in the analysis but also for some of the discarded lines there is a small difference in line strength. An example ca be seen in the first panel in Fig. 4 where the observed line is stronger than the synthetic. One reason is incorrect abundances but another is departure from local thermodynamic equilibrium (non-LTE effects). This is especially true for the Sun as the conditions in the atmosphere allow for departure from LTE for a significant amount of elements. In Fig. 8 in Lind & Amarsi (2024) we can see that a Ca line in the optical wavelength region is clearly affected by non-LTE effects where the 1D non-LTE line is deeper than the LTE line. We also note that the 3D LTE line is deeper than the 3D non-LTE line, which indicates that the 1D models are missing some physics. No investigation of non-LTE effects for Ca in M dwarfs has been done to the knowledge of the authors. M dwarfs are assumed to be in LTE but can be affected by non-LTE as shown in Olander et al. (2021), where abundance corrections of up to 0.2 dex were found for K. Non-LTE effects for Ti were investigated in Hauschildt et al. (1997) who found a clear difference between LTE and non-LTE. Nordmeier (2020) found an abundance correction of 0.1 dex between LTE and non-LTE. It is clear that non-LTE needs to be thoroughly investigated for M dwarfs.

In the future we should explore the inclusion of molecular lines when fitting in order to derive abundances of various elements. Souto et al. (2022) used H_2O and OH molecules in order to find O abundances. It was also used to derive T_{eff} and $\log g$. Souto et al. (2020) found that using FeH lines does not give the same [Fe/H] as using atomic Fe lines. They estimated a difference of 0.12 dex between [Fe/H] from Fe I and FeH lines in the H band. In our analysis of the star GJ 699 we found it difficult to derive [Fe/H] as the Fe I lines were weak. When inspecting Fig. 2 in Souto et al. (2020) we can see that the stars with lower T_{eff} and [Fe/H] have a better agreement between [Fe/H] obtained from Fe I lines and from FeH lines. This means that if we have a first estimate of the iron abundance and the star is cool we could use FeH lines as well as Fe I lines. This could possibly lower the uncertainty of [Fe/H] in cool, low-metallicity stars such as GJ 699. A more extended investigation is needed in order to test this. FeH lines could also be used to obtain other parameters such as T_{eff}, as shown in Lindgren et al. (2016); Lindgren & Heiter (2017).

References

Abia, C., Tabernero, H. M., Korotin, S. A., et al. 2020, A&A, 642, A227
Alvarez, R. & Plez, B. 1998, A&A, 330, 1109
Bergemann, M., Hoppe, R., Semenova, E., et al. 2021, MNRAS, 508, 2236
Bergemann, M., Kudritzki, R.-P., Plez, B., et al. 2012, ApJ, 751, 156
Berger, D. H., Gies, D. R., McAlister, H. A., et al. 2006, ApJ, 644, 475
Birky, J., Hogg, D. W., Mann, A. W., & Burgasser, A. 2020, ApJ, 892, 31
Blanco-Cuaresma, S. 2019, MNRAS, 486, 2075
Blanco-Cuaresma, S., Soubiran, C., Heiter, U., & Jofré, P. 2014, A&A, 569, A111
Boyajian, T. S., von Braun, K., van Belle, G., et al. 2012, ApJ, 757, 112
Brinkman, C. L., Polanski, A. S., Huber, D., et al. 2024, AJ, 168, 281
Butler, R. P., Marcy, G. W., Williams, E., et al. 1996, PASP, 108, 500
Caballero, J. A., González-Álvarez, E., Brady, M., et al. 2022, A&A, 665, A120
Cadieux, C., Doyon, R., Plotnykov, M., et al. 2022, AJ, 164, 96
Dressing, C. D. & Charbonneau, D. 2015, ApJ, 807, 45
Ellis, T. 2022, PhD thesis, LSU
Fouqué, P., Moutou, C., Malo, L., et al. 2018, MNRAS, 475, 1960
Gerber, J. M., Magg, E., Plez, B., et al. 2023, A&A, 669, A43
Gray, R. O. & Corbally, Christopher, J. 2009, Stellar Spectral Classification (Princeton University Press)
Gustafsson, B. 1989, ARA&A, 27, 701
Gustafsson, B., Edvardsson, B., Eriksson, K., et al. 2008, A&A, 486, 951
Hauschildt, P. H., Allard, F., Alexander, D. R., & Baron, E. 1997, ApJ, 488, 428
Henry, T. J., Jao, W.-C., Subasavage, J. P., et al. 2006, AJ, 132, 2360
Henry, T. J. & McCarthy, Donald W., J. 1993, AJ, 106, 773
Ishikawa, H. T., Aoki, W., Hirano, T., et al. 2022, AJ, 163, 72
Jahandar, F., Doyon, R., Artigau, É., et al. 2025, ApJ, 978, 154
Jönsson, H., Holtzman, J. A., Allende Prieto, C., et al. 2020, AJ, 160, 120
Kervella, P., Mérand, A., Ledoux, C., Demory, B. O., & Le Bouquin, J. B. 2016, A&A, 593, A127
Köhler, J. & viper Pipeline Team. 2024, VIPER Manual, ESO, Garching bei München, Germany, https://mzechmeister.github.io/viper_RV_pipeline/
Kurucz, R. L. 2007, Robert L. Kurucz on-line database of observed and predicted atomic transitions, http://kurucz.harvard.edu/atoms/2000/
Kurucz, R. L. 2014, Robert L. Kurucz on-line database of observed and predicted atomic transitions, http://kurucz.harvard.edu/atoms/2600/
Kurucz, R. L. 2016, Robert L. Kurucz on-line database of observed and predicted atomic transitions, http://kurucz.harvard.edu/atoms/2200/
Lawler, J. E., Guzman, A., Wood, M. P., Sneden, C., & Cowan, J. J. 2013, ApJS, 205, 11
Lind, K. & Amarsi, A. M. 2024, ARA&A, 62, 475
Lindgren, S. & Heiter, U. 2017, A&A, 604, A97
Lindgren, S., Heiter, U., & Seifahrt, A. 2016, A&A, 586, A100
Loyd, P., Schreyer, E., Owen, J., et al. 2024, in AAS/Division for Extreme Solar Systems Abstracts, Vol. 56, AAS/Division for Extreme Solar Systems Abstracts, 625.22
Luque, R., Serrano, L. M., Molaverdikhani, K., et al. 2021, A&A, 645, A41
Magg, E., Bergemann, M., Serenelli, A., et al. 2022, A&A, 661, A140
Majewski, S. R., Schiavon, R. P., Frinchaboy, P. M., et al. 2017, AJ, 154, 94
Maldonado, J., Micela, G., Baratella, M., et al. 2020, A&A, 644, A68
Mann, A. W., Feiden, G. A., Gaidos, E., Boyajian, T., & von Braun, K. 2015, ApJ, 804, 64
Melo, E., Souto, D., Cunha, K., et al. 2024, ApJ, 973, 90
Nordmeier, N. 2020, Three dimensional spectroscopic NLTE abundance corrections of Sodium and Titanium in M-dwarfs, Bachelor thesis, University of Heidelberg
O'Brian, T. R., Wickliffe, M. E., Lawler, J. E., Whaling, W., & Brault, J. W. 1991, Journal of the Optical Society of America B Optical Physics, 8, 1185, (BWL)
Olander, T., Gent, M. R., Heiter, U., et al. 2025, A&A, 696, A62
Olander, T., Heiter, U., & Kochukhov, O. 2021, A&A, 649, A103
Origlia, L., Oliva, E., Baffa, C., et al. 2014, in Society of Photo-Optical Instrumentation Engineers (SPIE) Conference Series, Vol. 9147, Ground-based and Airborne Instrumentation for Astronomy V, ed. S. K. Ramsay, I. S. McLean, & H. Takami, 91471E

Pakhomov, Y. V., Ryabchikova, T. A., & Piskunov, N. E. 2019, Astronomy Reports, 63, 1010

Passegger, V. M., Bello-García, A., Ordieres-Meré, J., et al. 2022, A&A, 658, A194

Passegger, V. M., Bello-García, A., Ordieres-Meré, J., et al. 2020, A&A, 642, A22

Passegger, V. M., Reiners, A., Jeffers, S. V., et al. 2018, A&A, 615, A6

Passegger, V. M., Schweitzer, A., Shulyak, D., et al. 2019, A&A, 627, A161

Piskunov, N., Wehrhahn, A., & Marquart, T. 2021, A&A, 646, A32

Piskunov, N. E., Kupka, F., Ryabchikova, T. A., Weiss, W. W., & Jeffery, C. S. 1995, A&AS, 112, 525

Piskunov, N. E. & Valenti, J. A. 2002, A&A, 385, 1095

Plez, B. 2012, Turbospectrum: Code for spectral synthesis, Astrophysics Source Code Library, record ascl:1205.004

Rabus, M., Lachaume, R., Jordán, A., et al. 2019, MNRAS, 484, 2674

Rains, A. D., Nordlander, T., Monty, S., et al. 2024, MNRAS, 529, 3171

Rajpurohit, A. S., Allard, F., Rajpurohit, S., et al. 2018, A&A, 620, A180

Rauer, H., Aerts, C., Cabrera, J., et al. 2024, arXiv e-prints, arXiv:2406.05447

Rauer, H., Catala, C., Aerts, C., et al. 2014, Experimental Astronomy, 38, 249

Reiners, A., Mrotzek, N., Lemke, U., Hinrichs, J., & Reinsch, K. 2016, A&A, 587, A65

Reiners, A., Zechmeister, M., Caballero, J. A., et al. 2018, A&A, 612, A49

Ryabchikova, T., Piskunov, N., Kurucz, R. L., et al. 2015, Physica Scripta, 90, 054005

Saloman, E. B. 2012, Journal of Physical and Chemical Reference Data, 41, 013101, sal12a

Santerne, A., Brugger, B., Armstrong, D. J., et al. 2018, Nature Astronomy, 2, 393

Sarmento, P., Rojas-Ayala, B., Delgado Mena, E., & Blanco-Cuaresma, S. 2021, A&A, 649, A147

Schaefer, G. H., White, R. J., Baines, E. K., et al. 2018, ApJ, 858, 71

Shan, Y., Reiners, A., Fabbian, D., et al. 2021, A&A, 654, A118

Smette, A., Sana, H., Noll, S., et al. 2015, A&A, 576, A77

Souto, D., Cunha, K., Smith, V. V., et al. 2020, ApJ, 890, 133

Souto, D., Cunha, K., Smith, V. V., et al. 2022, ApJ, 927, 123

Storm, N. & Bergemann, M. 2023, MNRAS, 525, 3718

Thiabaud, A., Marboeuf, U., Alibert, Y., Leya, I., & Mezger, K. 2015, A&A, 580, A30

Tsuji, T. & Nakajima, T. 2016, PASJ, 68, 13

van Leeuwen, F. 2007, A&A, 474, 653

von Braun, K., Boyajian, T. S., Kane, S. R., et al. 2011, ApJ, 729, L26

von Braun, K., Boyajian, T. S., van Belle, G. T., et al. 2014, MNRAS, 438, 2413

Wang, H. S., Liu, F., Ireland, T. R., et al. 2019, MNRAS, 482, 2222

Woolf, V. M. & Wallerstein, G. 2005, MNRAS, 356, 963

Zechmeister, M., Köhler, J., & Chamarthi, S. 2021, viper: Velocity and IP EstimatoR, Astrophysics Source Code Library, record ascl:2108.006

Appendix A: Line data and lines fitted for each star

In this appendix we present the atomic data for the spectral lines used in the analysis in Table A.1. We also specify which lines were fitted for each star. Table A.2 shows the Fe lines, Table A.3 shows the Ti lines, and Table A.4 shows the Ca lines. In the latter three tables, the leftmost column indicates the rest wavelength in air of each line in Å. There is one column for each star in the analysis where an "X" marks if a line was used or not. These tables are referred to in Sect. 3.1.

Table A.1. Atomic data for the spectral lines used in the analysis.

Species	λ_{air} [Å]	E_{low} [eV]	$\log gf$	$\log \gamma_{\text{rad}}$	$\log \gamma_{\text{Waals}}$	References
Fe	10340.885	2.1979	-3.577	7.250	-7.800	K14
Ca	10343.819	2.9325	-0.300	8.500	-7.480	K07
Fe	10395.794	2.1759	-3.393	7.260	-7.800	K14
Ti	10396.800	0.8484	-1.539	5.140	-7.810	K16
Fe	10423.027	2.6924	-3.616	6.130	-7.810	K14
Fe	10423.743	3.0713	-2.918	6.740	-7.790	K14
Fe	10435.355	4.7331	-1.945	8.350	-7.550	K14
Fe	10469.652	3.8835	-1.184	6.830	-7.820	K14
Ti	10496.116	0.8360	-1.651	5.130	-7.810	K16
Fe	10532.234	3.9286	-1.480	6.820	-7.820	K14
Ca	10558.425	4.5541	-0.731	7.330	-6.960	K07
Fe	10577.139	3.3014	-3.136	7.960	-7.770	K14
Ti	10584.634	0.8259	-1.775	5.130	-7.810	K16
Ti	10607.716	0.8484	-2.697	5.130	-7.810	K16
Fe	10616.721	3.2671	-3.127	7.990	-7.780	K14
Ti	10661.623	0.8181	-1.915	5.130	-7.810	K16
Ti	10732.865	0.8259	-2.515	5.130	-7.810	K16
Ti	10774.866	0.8181	-2.666	5.130	-7.810	K16
Fe	10783.050	3.1110	-2.567	6.740	-7.790	K14
Fe	10818.274	3.9597	-1.948	6.820	-7.820	K14
Ca	10827.013	4.8770	-0.300	8.220	-6.930	K07
Ca	10838.970	4.8775	0.238	8.400	-7.590	K07
Ca	10861.582	4.8767	-0.343	8.390	-7.590	K07
Fe	10863.518	4.7331	-0.895	8.350	-7.550	K14
Fe	10884.262	3.9286	-1.925	6.830	-7.820	K14
Fe	10896.299	3.0713	-2.694	6.880	-7.790	K14
Fe	11607.572	2.1979	-2.009	7.160	-7.820	BWL, K14
Ca	11759.570	4.5313	-0.878	7.500	-7.090	K07
Ca	11769.345	4.5322	-1.011	7.500	-7.090	K07
Fe	11884.083	2.2227	-2.083	7.160	-7.820	BWL, K14
Ca	11955.955	4.1308	-0.849	8.010	-7.300	K07
Fe	12227.112	4.6070	-1.368	8.430	-7.540	K14
Fe	12342.916	4.6382	-1.463	8.420	-7.540	K14
Ti	12600.277	1.4432	-2.320	6.810	-7.790	LGWSC, Sal12a, K16
Fe	12807.152	3.6398	-2.452	8.080	-7.750	K14
Ti	12811.478	2.1603	-1.390	7.990	-7.750	LGWSC, Sal12a, K16
Ca	12816.045	3.9104	-0.765	8.280	-7.520	K07
Ti	12821.672	1.4601	-1.190	6.810	-7.790	LGWSC, Sal12a, K16
Ca	12823.867	3.9104	-0.997	8.280	-7.520	K07
Fe	12824.859	3.0176	-3.835	6.070	-7.810	K14
Ca	12827.059	3.9104	-1.478	8.280	-7.520	K07
Ti	12831.445	1.4298	-1.490	6.820	-7.790	LGWSC, Sal12a, K16
Fe	12840.574	4.9556	-1.329	8.710	-7.550	K14
Fe	12879.766	2.2786	-3.458	7.170	-7.820	BWL, K14
Ca	12909.070	4.4300	-0.224	7.770	-7.710	K07
Ti	13011.897	1.4432	-2.270	6.820	-7.790	LGWSC, Sal12a, K16
Ca	13033.554	4.4410	-0.064	7.770	-7.710	K07
Ca	13057.885	4.4410	-1.092	7.770	-7.710	K07

Notes. All lines are from neutral atomic species (i.e., Fe I, Ca I, Ti I). λ ... wavelength, E_{low} ... lower level energy, $\log gf$ ... logarithm (base 10) of the product of the oscillator strength of the transition and the statistical weight of the lower level, $\log \gamma_{\text{rad}}$ ... logarithm of the radiative damping width in units of rad s^{-1}, $\log \gamma_{\text{Waals}}$ ... logarithm of the van der Waals broadening width per unit perturber number density at 10 000 K in units of rad s^{-1} cm^3. Unknown damping parameters are set to zero.

References. BWL ... O'Brian et al. (1991), K07 ... Kurucz (2007), K14 ... Kurucz (2014), K16 ... Kurucz (2016), LGWSC ... Lawler et al. (2013), Sal12a ... Saloman (2012).

Table A.2. Fitted Fe I lines.

λ_{air} [Å]	GJ 411	GJ 412A	GJ 436	GJ 526	GJ 581	GJ 699	GJ 725A	GJ 725B	GJ 809
10340.885	X	X	X	X	X				X
10395.794	X	X	X	X	X		X		X
10423.027	X		X	X	X	X	X	X	X
10423.743			X		X			X	X
10435.355	X	X	X	X	X	X			X
10469.652	X	X	X	X		X	X	X	X
10532.234	X	X	X	X	X			X	X
10577.139				X	X			X	X
10616.721				X					X
10783.050	X	X	X	X	X	X	X	X	X
10818.274				X					X
10863.518							X		
10884.262				X					X
10896.299	X	X	X	X	X		X		X
11607.572					X				
11884.083	X	X	X		X	X	X	X	X
12227.112	X			X			X	X	X
12342.916				X					X
12807.152	X	X	X	X	X	X	X	X	X
12824.859				X					X
12840.574									X
12879.766	X	X	X	X	X	X	X	X	

Table A.3. Fitted Ti I lines.

λ_{air} [Å]	GJ 411	GJ 412A	GJ 436	GJ 526	GJ 581	GJ 699	GJ 725A	GJ 725B	GJ 809
10396.800	X	X	X	X	X	X	X	X	X
10496.116	X	X	X	X	X	X	X	X	X
10584.634					X				
10607.716	X	X	X	X	X	X	X	X	X
10661.623	X	X	X	X	X	X		X	X
10732.865	X	X	X	X	X	X	X	X	X
10774.866	X	X	X	X	X	X		X	X
12600.277	X	X	X	X	X	X	X	X	X
12811.478	X	X	X	X	X	X	X	X	X
12821.672	X	X	X	X	X	X	X	X	X
12831.445	X	X	X	X	X	X	X	X	X
13011.897			X			X	X		

Table A.4. Fitted Ca I lines.

λ_{air} [Å]	GJ 411	GJ 412A	GJ 436	GJ 526	GJ 581	GJ 699	GJ 725A	GJ 725B	GJ 809
10343.819	X	X	X	X	X	X	X	X	X
10558.425			X		X				
10827.013		X		X					
10838.970	X	X	X	X	X		X		X
10861.582				X	X			X	X
11759.570	X								
11769.345					X		X	X	
11955.955	X	X	X	X	X		X	X	X
12816.045						X			
12823.867	X	X	X	X	X	X	X	X	X
12827.059	X		X	X	X		X	X	X
12909.070	X	X	X	X	X	X	X	X	X
13033.554	X	X	X	X	X	X	X	X	X
13057.885				X		X		X	X